Sensors & Diagnostics

PAPER

View Article Online
View Journal | View Issue

Cite this: *Sens. Diagn.*, 2023, **2**, 445

An electrochemiluminescent sensor based on hydrophilic $CsPbBr_3$/TDPA nanocrystals for sensitive detection of nitrobenzene

Wen-Xu Zhang, Jing-Shuai Chen, Xing-Pei Liu,*
Chang-Jie Mao * and Bao-Kang Jin

Received 6th January 2023,
Accepted 7th February 2023

DOI: 10.1039/d3sd00007a

rsc.li/sensors

The extreme sensitivity of perovskite nanoparticles to water has seriously hindered their application. At present, all inorganic perovskite nanocrystals (NCs) have received extensive attention due to their excellent photoelectric properties. A highly hydrophilic composite $CsPbBr_3$/TDPA NCs was synthesized in the presence of oleylamine molecules, which greatly enhanced its water stability. The electrochemiluminescence (ECL) intensity and stability of the composites are much higher than those of single $CsPbBr_3$ quantum dots (QDs). For the first time, we have developed a sensor for the specific detection of nitrobenzene using the ECL method. It was found that nitrobenzene could significantly enhance the ECL signal of $CsPbBr_3$/TDPA NCs. The ECL sensor showed a good linear relationship with the concentration of nitrobenzene in the range of 1 mM to 0.1 μM, and the detection limit was as low as 0.05 μM (S/N = 3). This work provides a new idea for the development of nitrobenzene ECL sensors.

With the development of science and technology, environmental pollution is becoming more and more serious due to the mass production and wide application of various chemical raw materials. Nitrobenzene compounds are widely used in chemical raw materials. For example, nitrobenzene is used in the manufacture of explosives, fuels, pesticides, drugs and other raw materials.[1] There are also some enterprises that use nitrobenzene as a solvent, used in coatings, shoes, floor materials and other production activities.[2] However, nitrobenzene can poison people and animals, damage the blood circulation and nervous system, and cause anemia and even death.[3] Nitrobenzene is usually stable in water due to the strong electron-absorbing properties of the nitro group of the aromatic ring.[4] The detection methods of nitrobenzene mainly include fluorescence (FL)[5] and scanning tunneling microscope break junction technique (STM-BJ).[6] Nevertheless, these methods may lack a certain degree of sensitivity and their costs are not easily estimated. At present, the ECL detection method of nitrobenzene has not been reported. ECL analysis technology is widely used in the detection field because of its advantages of low detection limit and high sensitivity.

Due to their excellent photoelectric properties, lead halide perovskites have attracted extensive attention in recent years. Perovskite is a direct bandgap semiconductor and has excellent carrier transport characteristics, and its optical bandgap can be adjusted by changing the type and proportion of halogen atoms.[7] At present, all inorganic perovskite nanocrystals (NCs) have been widely used in the preparation of high-efficiency solar cells,[8] light-emitting diodes,[9] lasers[10] and photodetectors.[11] They also have many applications in the field of analysis and testing, such as fluorescent probes,[12] ECL,[13] photoelectric chemistry[14] and so on. However, the stability of all inorganic perovskite nanoparticles is poor, especially in water, which greatly limits their practical application. Ligand engineering and coating with inert shells have proved to be effective methods to improve the stability of perovskites. In the absence of any amines, ligands reduce non-radioactive recombination pathways from surface defects. Therefore, oleamine ligands were identified to contribute to reaction kinetics. They have the ability to interact with the surface of cesium bromide NCs through the formation of hydrogen bonds, *via* either direct ligand addition or substitution of the surface Cs^+ cations. Alkyl phosphinic acids, which have a strong affinity for Pb^{2+}, contain two chelating sites that allow the ligand to interact strongly with the surface of perovskite nanoparticles and have been used to replace oleic acid.[15] For example, Kovalenko *et al.* first prepared $CsPbX_3$ perovskite NCs by hot injection of cesium stearate in $PbBr_2$ solution at 170 °C with the assistance of long-chain organic ligands such as octadecene and oleylamine.[16] Wu *et al.* synthesized sodium (Na) passivated $CsPbBr_3$ nanocrystals at room temperature

---

Key Laboratory of Structure and Functional Regulation of Hybrid Materials (Ministry of Education), School of Chemistry and Chemical Engineering, Anhui University, Hefei, Anhui 230601, China. E-mail: 414043594@qq.com, maochangjie@sina.com

using a modified ligand-assisted reprecipitation method and dispersed them in water/*n*-hexane solution.[17] However, after some surface modification, they still have inherent fragility in terms of stability. This not only hinders the application of perovskite NCs in photochemistry, but also becomes a major obstacle to their future application in electrochemiluminescence.

Electrochemiluminescence (ECL) is a kind of light radiation produced by electrochemically induced energy relaxation of excited states.[18] It has the advantages of high sensitivity, low background signal and easy control.[19] $CsPbBr_3$ QDs have excellent photoelectric performance, and many researchers have begun to explore their ECL performance. Zhu *et al.* obtained strong and stable ECL from $CsPbBr_3$ QDs by hydrolyzing tetramethyl orthosilicate while encapsulating $CsPbBr_3$ QDs and a coreactant (CoR) into an *in situ* generated SiO_2 matrix.[20] Wang *et al.* used hydrogen peroxide as the co-reactive agent for the first time to investigate the charge transfer related anodic redox and ECL of all-inorganic perovskite $CsPbBr_3$ NCs in aqueous media.[21] However, most studies based on $CsPbBr_3$ QDs only focus on anode ECL, and there are few reports on cathode ECL of perovskites. Cathodic ECL also has unique advantages, such as expanding the possible types of ECL reactions, eliminating the oxidation products of the emitter, and reducing the interference of compounds present in the sample.[22] Therefore, it is of great significance to explore the cathode ECL properties of all inorganic perovskites.

The application of self-assembled alkyl phosphate monolayers on metal or metal oxide surfaces has been used as a stabilization method to protect metal surfaces and interfaces against corrosion.[23] In this work, we synthesized tetradecylphosphonic acid (TDPA) coated $CsPbBr_3$ nanocrystals by supersaturated crystallization rather than by hot injection. This method has the advantages of simple and controllable synthesis conditions, cost saving and easy to carry out large-scale synthesis. We systematically studied the cathodic ECL performance of $CsPbBr_3$/TDPA NCs in aqueous solution. The results show that the NCs still maintained good ECL performance after one week of dispersion in water. $CsPbBr_3$ QD based ECL analysis has been performed in the aqueous phase, expanding its application in biological analysis. Compared with pure $CsPbBr_3$ NCs, the material overcomes the luminescence instability defect of $CsPbBr_3$ QDs and has better ECL signal intensity. A series of classical semiconductor nanocrystals, such as CdSe,[24] CdS,[25] and ZnS,[26] have ECL emission characteristics. However, they have been criticized for the stability of their ECL response signal, especially the instability of NCs in the ECL process with high excitation electrochemical potential. Moreover, the low ECL signal intensity of some two-dimensional nanosheets also limits their application in ECL analysis. For example, the ECL emission of a g-C_3N_4 film rapidly degrades at the applied potential range of 0 to −1.5 V.[27] This can be ascribed to electrode passivation occurring immediately after one cyclic potential scan, leading to a sharp decrease in ECL emission at subsequent potential scans. Although a stable ECL signal can be obtained by using small cathodic potentials, the ECL intensity is apparently too weak for analytical application. Nevertheless, the combined action of TDPA and oleylamine molecules improved the surface defect state of $CsPbBr_3$ QDs and promoted the charge transfer recombination of quantum dots and excited states, as well as greatly enhancing the ECL signal intensity and luminescence stability. However, $CsPbBr_3$/TDPA NCs have not been used in the application of ECL research right now. This material overcomes the characteristics of poor conductivity of traditional $CsPbBr_3$ QDs, and has excellent electrochemical activity and electron transport ability. Moreover, nitrobenzene can specifically enhance the ECL signal of $CsPbBr_3$, which is believed to have broad development prospects.

Experimental section

Chemicals and materials

Caesium bromide (99.5%), lead bromide (99.0%), and oleylamine (OAm, 80–90%) were obtained from Aladdin. Toluene (99.8%) was purchased from Aldrich. *N*,*N*-Dimethylformamide (DMF, 99.8%), sodium chloride (AR, 99.5%), potassium chloride (99.5%), sodium phosphate dibasic (99.99% metals basis), potassium phosphate monobasic (99.5%), potassium persulfate (99.5%), nitrobenzene (AR, 99%), 1-tetradecylphosphonic acid (TDPA, 98%), and oleic acid (OA, AR) were obtained from Macklin.

Apparatus

X-ray polycrystalline diffractometer (XRD, Smartlab, 9 kW, Japan), X-ray photoelectron spectroscopy (XPS, ESCALAB 250, the United States), fluorescence spectrometer (PL, F-2500, Japan), Fourier transform infrared spectrometer (FTIR, NEXUS-870, Japan), ultraviolet visible absorption spectrometer (UV-1750, Shimadzu, Japan), scanning electron microscope (SEM, REGULUS8230, Japan), transmission electron microscope (TEM, JEM-2100, Japan). All electrochemical measurements were carried out on a CHI 660E electrochemical workstation (Shanghai CH Instrument Co., Ltd., China) and the measurements of electrochemiluminescence (ECL) were taken on an MPI-E electrochemiluminescence analyzer (Xi'An Remax Electronic Science & Technology Co. Ltd., Xi'An, China). During the test, a Ag/AgCl electrode was selected as the reference electrode, a platinum wire electrode as the auxiliary electrode and a glassy carbon electrode (GCE) as the working electrode. The photomultiplier tube voltage is set to 600 V. Electrochemical impedance spectroscopy (EIS) measurements were carried out on an AutoLab electrochemical analysis instrument (Holland).

Preparation of $CsPbBr_3$ QDs

Traditional $CsPbBr_3$ QDs were prepared according to methods reported in the literature.[28] In brief, 0.1 mmol of CsBr and 0.1 mmol of $PbBr_2$ were dissolved in 2 mL of DMF, and then 80 μL of OAm and 250 μL of OA were added with vigorous stirring. Then, strong green emission was observed when 200 μL precursor solution was dispersed into 3 mL toluene solvent.

Preparation of $CsPbBr_3$/TDPA NCs

$CsPbBr_3$/TDPA NCs were synthesized according to the literature.[29] Some details have been slightly changed. In brief, 0.1 mmol of CsBr, 0.1 mmol of $PbBr_2$, 25 mg of TDPA and 0.125 mL of OAm were dissolved in 2.5 mL of DMF and stirred vigorously. Then, 200 μL of the precursor solution was dispersed into 2 mL toluene solvent and centrifuged at 9000 rpm for 10 min. At last, the NCs were washed with cyclohexane several times, and dried in a vacuum drying oven. The synthesis process of $CsPbBr_3$/TDPA NCs is shown in Scheme 1(A).

Construction of the sensor

The assembly process of the sensor is shown in Scheme 1(B). Firstly, the glassy carbon electrode was polished with alumina powder, and then sonicated in ultrapure water, ethanol and ultrapure water, and finally the surface of the GCE was dried with nitrogen. 10 μL of 0.5 mg mL^{-1} $CsPbBr_3$/TDPA NCs were dropped on the electrode surface and dried in air for electrochemical testing. The prepared sensor was placed in 5 mL test liquid containing 0.12 M $K_2S_2O_8$ and 10 mM PBS (pH = 7.4). The scanning potential range varies from 0 to −2.0 V, the scanning rate is 100 mV s^{-1}, and the high voltage of the photomultiplier tube is set at 600 V.

Results and discussion

Morphological and structural characterization

Fig. 1A shows the TEM images of $CsPbBr_3$/TDPA NCs aqueous solution at the initial stage, in which the NCs presented the shape of regular nanocubes. In addition, the size uniformity of nanoparticles coated with TDPA and OAm is also fabulous. The high-resolution TEM (HR-TEM) image (Fig. 1B) of the NCs showed a *d*-spacing of 2.9 Å, which was consistent with the (200) crystal face of cubic phase $CsPbBr_3$.[30] As shown in Fig. 1C, the as-prepared $CsPbBr_3$ showed a nanoplate shape with good size uniformity.

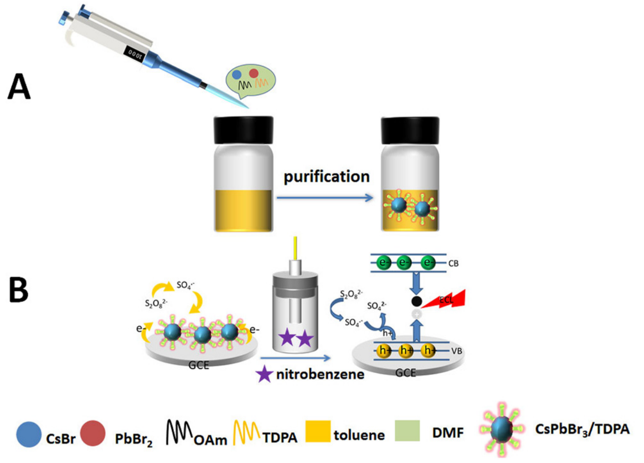

Scheme 1 (A) The synthesis process of $CsPbBr_3$/TDPA NCs. (B) Construction and detection of ECL sensors.

We further analyzed the crystal phase structure of $CsPbBr_3$/TDPA NCs powder by XRD, as shown in Fig. 2A. There are also broad peaks and some impurity peaks on the curve of $CsPbBr_3$/TDPA NCs, which can be confirmed as the peak of TDPA by comparing with the XRD spectrum of TDPA. At the same time, the main diffraction peaks of NCs correspond to the (100), (110), (200), (210), (211) and (202) crystal planes of cubic phase $CsPbBr_3$, respectively, indicating that the $CsPbBr_3$/TDPA NCs have a cubic crystal structure.[31] We further investigated the crystal structure changes of nanoparticles dispersed in water for different periods of time (Fig. 2B). After one or even 5 days of $CsPbBr_3$/TDPA NCs dissolution in water, the position of the XRD peaks almost did not change, indicating that the NCs basically maintained the original cubic phase structure. However, individual small peaks also appeared at $2\theta = 23.5°$ and $2\theta = 26.4°$, which may be due to the recrystallization of the nanoparticles in water, resulting in a change in crystal orientation. At the same time, the prepared materials were characterized by Fourier transform infrared spectroscopy, and the results are shown in Fig. 2C. Curve a is the infrared spectrum of $CsPbBr_3$/TDPA NCs, and curve b is the infrared spectrum of TDPA. By comparing the FTIR spectra of TDPA and $CsPbBr_3$/TDPA NCs, the peaks at 2933 cm^{-1} and 2858 cm^{-1} can be summed up as the characteristic stretching vibration peaks of C–H. Meanwhile, curve b shows that the peaks at 1000 cm^{-1} and 962 cm^{-1} can be attributed to the characteristic stretching vibration peaks of P–O–H.[32] Notably, curve a shows that the P=O tensile vibration at 1230 cm^{-1} is replaced by a broad peak at 1000–900 cm^{-1}, indicating that the P=O and P–O–H bonds gradually break and produce Pb–O–P bonds.[33] The successful synthesis of the NCs was confirmed. The UV-vis absorption spectra and photoluminescence spectra of the synthesized $CsPbBr_3$/TDPA NCs and $CsPbBr_3$ QDs solution are shown in Fig. 2D. The maximum absorption peak and fluorescence emission peak of $CsPbBr_3$/TDPA are located at 512 nm and 519 nm, respectively. The $CsPbBr_3$ QDs exhibit an absorption onset at 509 nm and an emission peak at 518 nm. A red shift was observed in $CsPbBr_3$ NCs in both cases of absorption and emission upon loading into TDPA, which may be attributed to an increase in the size of NCs after engaging with TDPA. In this work, we used TDPA and OAm as ligands and it was found that the fluorescence intensity of $CsPbBr_3$ synthesized with TDPA as the ligand was stronger than that with OA and OAm as ligands. This should be due to the more efficient surface passivation of $CsPbBr_3$ NCs by TDPA, resulting in reduced surface defect density.

The valence states of surface elements of $CsPbBr_3$/TDPA NCs were characterized by X-ray photoelectron spectroscopy. The results are shown in Fig. 3. Fig. 3A shows that the Cs, Pb, Br, C, N, O and P elements exist in $CsPbBr_3$/TDPA NCs. The peaks of Pb 4f are located at 143 and 138.1 eV,

© 2023 The Author(s). Published by the Royal Society of Chemistry

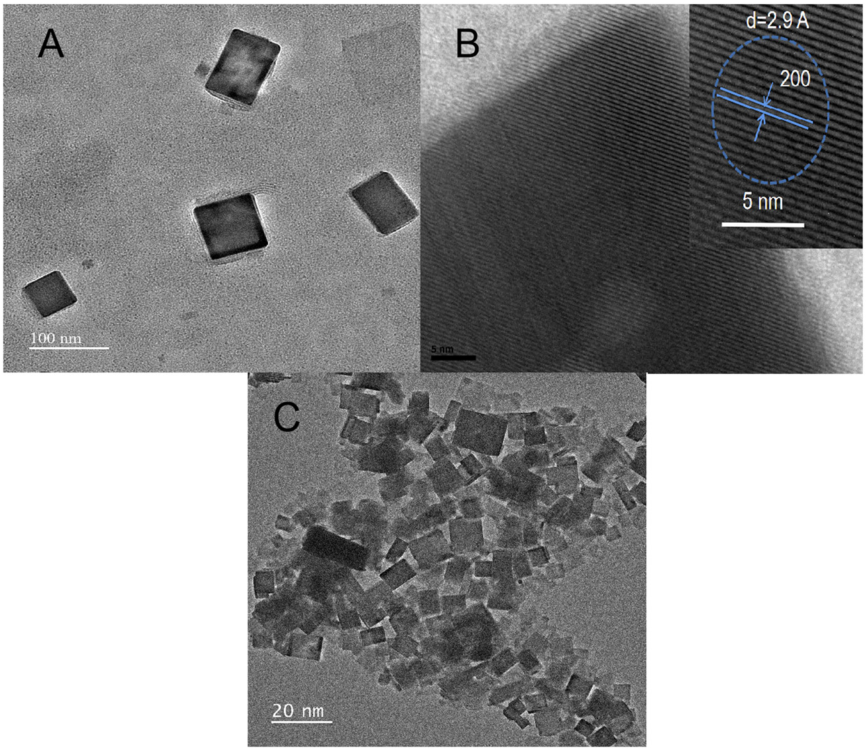

Fig. 1 The (A) TEM and (B) HR-TEM images of $CsPbBr_3$/TDPA NCs. (C) The TEM image of $CsPbBr_3$ QDs.

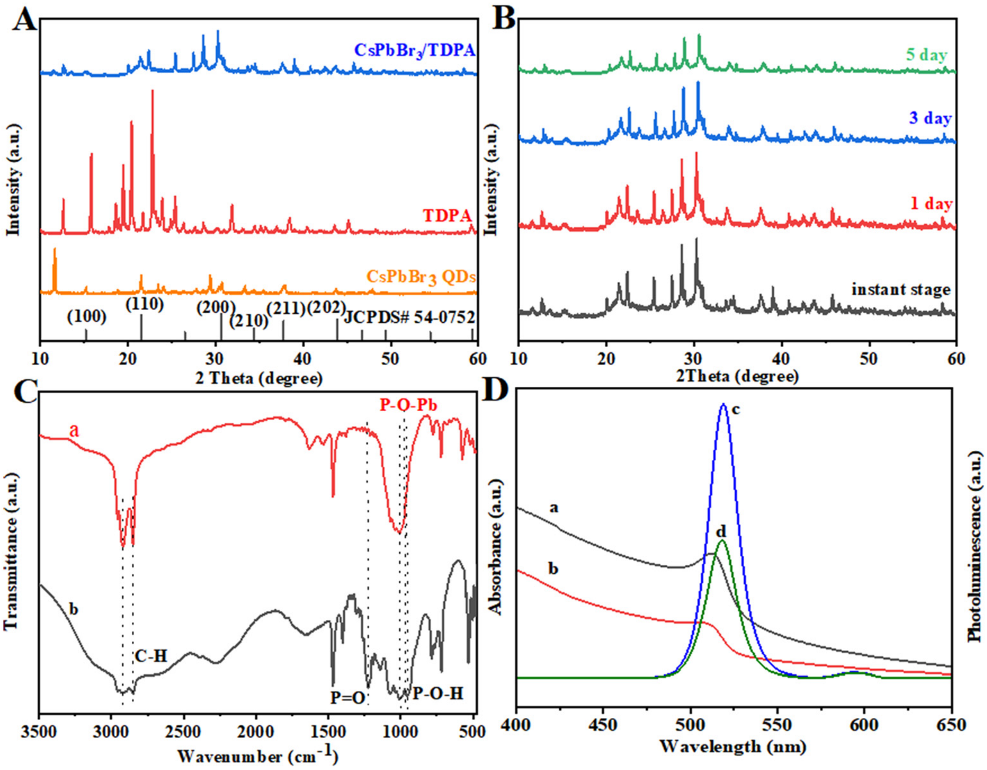

Fig. 2 (A) XRD patterns of TDPA, $CsPbBr_3$ QDs and $CsPbBr_3$/TDPA NCs. (B) XRD patterns of $CsPbBr_3$/TDPA NCs dispersed in water for different times. (C) The FTIR spectra of (a) $CsPbBr_3$/TDPA NCs and (b) TDPA. (D) Absorbance spectra of $CsPbBr_3$/TDPA NCs (a) and $CsPbBr_3$ QDs (b); photoluminescence spectra of $CsPbBr_3$/TDPA NCs (c) and $CsPbBr_3$ QDs (d).

corresponding to Pb $4f_{5/2}$ and Pb $4f_{7/2}$ in Fig. 3, respectively. Additionally, the Br 3d peaks could be fitted to two peaks ($3d_{5/2}$, $3d_{3/2}$) with binding energies of 68.4 and 69.4 eV (Fig. 3C). Meanwhile, the peaks of O 1s are located at 529.8,

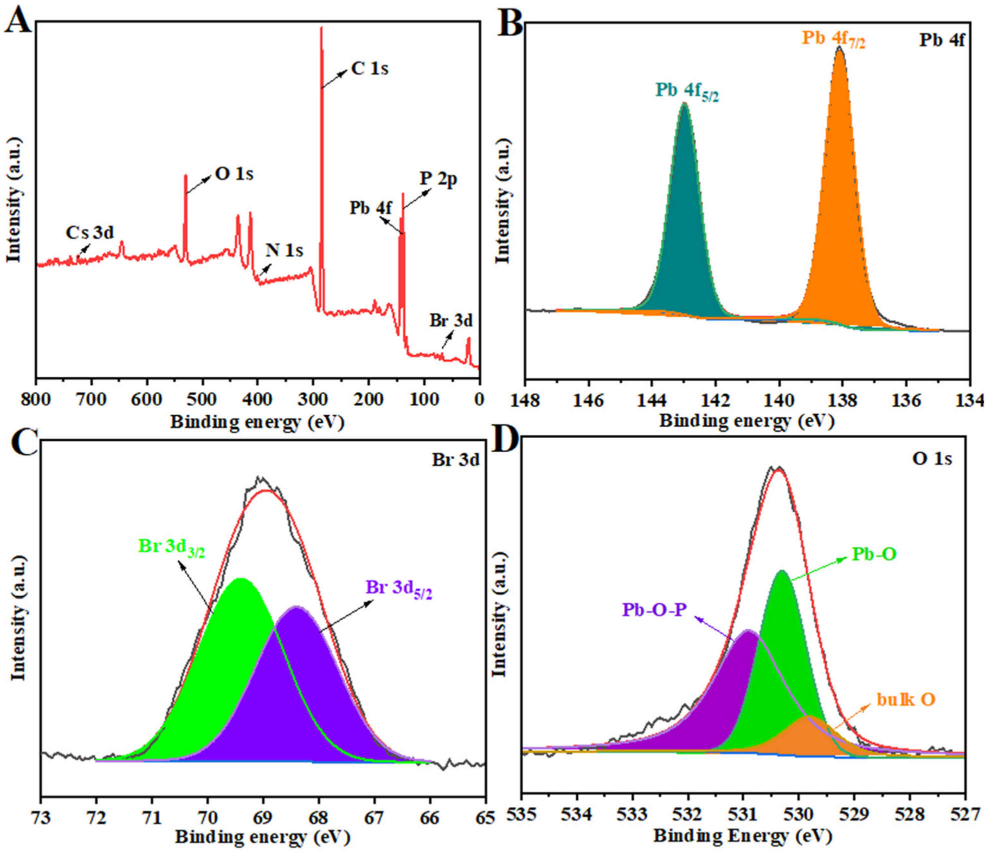

Fig. 3 XPS analysis of the full region of $CsPbBr_3$/TDPA NCs (A) and different elements Pb 4f (B), Br 3d (C), and O 1s (D).

530.3 and 530.9 eV (Fig. 3D), corresponding to bulk O, Pb–O, and Pb–O–P bonds in $CsPbBr_3$/TDPA NCs, respectively. The above results prove that we have successfully synthesized $CsPbBr_3$/TDPA NCs.

Stability of $CsPbBr_3$/TDPA NCs

Due to the poor stability of perovskite materials, it is difficult to maintain their original structure and optical properties due to the influence of environmental and interface factors. And the instability of perovskite-type nanomaterials in aqueous solution greatly limits their electrochemical applications. Therefore, the water stability of $CsPbBr_3$/TDPA NCs was investigated by measuring their ECL. The $CsPbBr_3$/TDPA NCs were dispersed in water until a clear homogeneous solution was formed. Then, 0.5 mg mL^{-1} aqueous $CsPbBr_3$/TDPA NCs solution was modified on a GCE to detect the ECL intensity at different periods. As shown in Fig. 4, after one

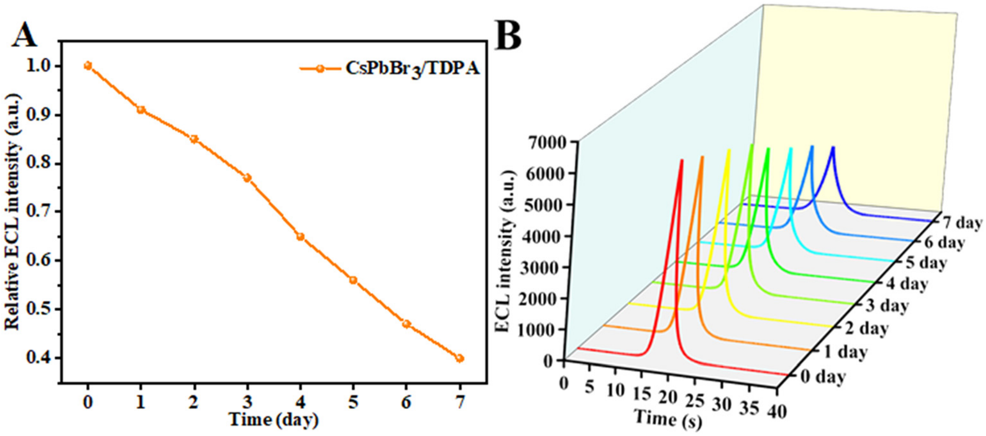

Fig. 4 (A) The relative ECL intensity of 0.5 mg mL^{-1} NCs as a function of time in water. (B) Effects of aqueous storage time on the ECL peak intensity of $CsPbBr_3$/TDPA NCs|GCE.

day of $CsPbBr_3$/TDPA NCs dispersion in water, the ECL intensity still remained at 90% of the initial intensity. Compared to a previous study,[34] it is worth noting that after a week of dispersion in water, the ECL intensity of the NCs was still 40% of the initial intensity, indicating that the water stability of the NCs was excellent. We conclude that the combined action of TDPA and OAm can improve the water stability of ECL and play an important role in delaying the degradation rate of $CsPbBr_3$ NCs in water.

Feasibility of electrochemical sensors

In order to further explore the feasibility of the constructed sensor, electrochemical impedance spectroscopy (EIS), cyclic voltammetry (CV) and ECL tests were used to characterize the modification process of the electrode surface. EIS was used to monitor the changes of interface properties of different electrode surfaces with 0.05 mmol L^{-1} $Fe(CN)_6^{3-/4-}$. The impedance spectrum includes a semicircle part and a linear part. The semi-circular part with higher frequency corresponds to the electron transfer limiting process, while the linear part with lower frequency represents the diffusion limiting process.[35] The bare GCE has the smallest impedance value (curve a, Fig. 5A), indicating that the GCE has good electrical conductivity. The resistance of the GCE modified by $CsPbBr_3$ QDs (Fig. 5B) is very large, indicating that its electrical conductivity is very poor. Compared with the bare GCE, the TDPA-modified GCE had higher impedance values (curve c in Fig. 5A). This is because TDPA, as a long organic small molecule, has a low electrical conductivity. Notably, the electron transfer resistance of $CsPbBr_3$/TDPA NCs was significantly reduced after surface modification of the GCE. The alkyl phosphonic acid and perovskite divalent cations (lead ions) have a strong interaction, and the change of the Pb–Br skeleton structure and composition mainly regulates the electronic properties. When TDPA interacts with the perovskite, the interface of the $CsPbBr_3$/TDPA NCs creates an electric potential that results in the spatial separation of carriers at the interface, which prevents the photoinduced radiative recombination of carriers and results in changes in their electrochemical properties. The results show that the prepared nanoparticles have very efficient electron transfer and excellent electrochemical activity. Fig. 5C shows the CV responses of the different modified electrodes. The exposed glassy carbon electrode (curve a) shows a pair of obvious $Fe(CN)_6^{3-/4-}$ redox peaks, indicating its excellent electron transport capacity. After modification of $CsPbBr_3$/TDPA NCs on the electrode surface (curve b), the peak current of the $Fe(CN)_6^{3-/4-}$ redox pair decreased slightly. When TDPA was modified on the electrode surface (curve c), the separation degree of redox peaks gradually increased, and the peak current decreased successively. In particular, the anode peak and

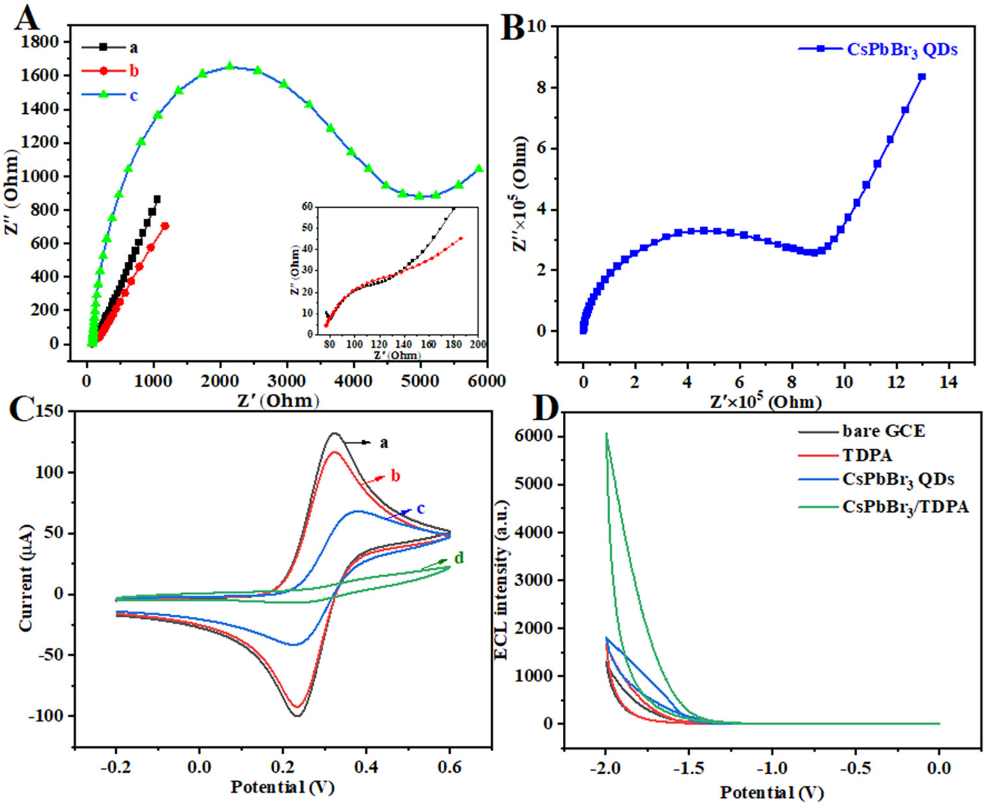

Fig. 5 (A) EIS characterization of (a) bare GCE, (b) $CsPbBr_3$/TDPA NCs and (c) TDPA. (B) EIS characterization of $CsPbBr_3$ QDs. (C) CV characterization of (a) bare GCE, (b) $CsPbBr_3$/TDPA NCs, (c) TDPA and (d) $CsPbBr_3$ QDs. (D) ECL–potential curves of the different modified electrodes.

cathode peak significantly decreased when the electrode is modified by $CsPbBr_3$ QDs (curve d), which just corresponds to the EIS results.

At present, the ECL properties of all inorganic perovskite nanocrystals are mostly concentrated on anodic ECL, and some related reports have shown that the ECL intensity of these materials in organic phases is very low. In this experiment, we measured the ECL response of a GCE modified at each step using $K_2S_2O_8$ as a coreactant (Fig. 5D). As expected, the ECL response of bare GCE is small and negligible. However, it is worth noting that weak ECL emission can be observed in $CsPbBr_3$ QDs|GCE. Moreover, after loading TDPA on the surface of the GCE, relatively weak ECL emission can also be observed due to its weak conductivity as a small organic molecule. Under the combined action of OAm and TDPA, a strong ECL signal was obtained at $CsPbBr_3$/TDPA|GCE. Compared to that of unmodified $CsPbBr_3$ QDs, the ECL signal intensity of $CsPbBr_3$/TDPA is significantly increased by about 3.4 times, and the ECL luminous efficiency is greatly improved.

ECL mechanism of electrochemical sensors

Hole and electron injection processes play an important role in the generation of ECL of $CsPbBr_3$ NCs. In previous reports, $CsPbBr_3$ NCs or their redox products may interact with $S_2O_8^{2-}$ to promote the generation of cathodic electrochemical luminescence. Therefore, we hypothesized that the ECL emission mechanism is caused by electron transfer annihilation between the $SO_4^{\bullet-}$ oxidation product $CsPbBr_3$/TDPA$^+$ and the electroreduction product $CsPbBr_3$/TDPA$^-$. Subsequently, the electron transfer produces an excited state $CsPbBr_3$/TDPA*, which is then relaxed by emission. The possible ECL mechanisms are as follows:[36]

$$S_2O_8^{2-} + e^- \rightarrow SO_4^{2-} + SO_4^{\bullet-}$$

$$SO_4^{\bullet-} + CsPbBr_3/TDPA \rightarrow SO_4^{2-} + CsPbBr_3/TDPA^+$$

$$CsPbBr_3/TDPA + e^- \rightarrow CsPbBr_3/TDPA^-$$

$$CsPbBr_3/TDPA^+ + CsPbBr_3/TDPA^- \rightarrow CsPbBr_3/TDPA^*$$

$$CsPbBr_3/TDPA^* \rightarrow CsPbBr_3/TDPA + h\nu$$

Based on previous reports, there is an interaction between perovskite colloidal particles and nitrobenzene.[37] π-Conjugated molecules tend to have excellent electrical conductivity, and good rigidity and planarity, due to the existence of π-electrons. It was found that the introduction of conjugated groups can greatly increase the contribution of organic components to the band edge, and reduce the narrow band gap to a certain extent, so as to promote the electronic coupling between the inorganic and organic layers of low-dimensional perovskites, and further promote the carrier transport.[38] Nitrobenzene is a compound rich in π-electrons, and its nitro group has a π–π interaction with the benzene ring. There is a strong interaction of π electrons between such conjugated molecules and the perovskite octahedron, that is, the nitrocellulose group can interact with the $PbBr_6$ cage of the perovskite, which may produce a passivation effect and promote the phase stability of the low-dimensional perovskite. The phenyl group is hydrophobic and has the potential to prevent water from entering. Therefore, in the process of continuous ECL scanning, the interaction between the redox products of $CsPbBr_3$/TDPA and $S_2O_8^{2-}$ is further promoted due to the effect of defect passivation and water osmosis inhibition. This process results in more and more catalytic products in the electrolyte, and also increases the contact area with $K_2S_2O_8$. Fig. 6 depicts the CV responses of bare GCE and $CsPbBr_3$/TDPA in an air-saturated water medium with $K_2S_2O_8$ as a coreactant. The obvious reduction peak of bare GCE at −0.97 V indicates that the strong oxidant $SO_4^{\bullet-}$ is formed by electrochemical reduction of $S_2O_8^{2-}$. Compared with that of the GCE, the reduction current of the $CsPbBr_3$/TDPA modified electrode was significantly increased in the presence of nitrobenzene, and the reduction potential was −0.74 V, which confirmed that nitrobenzene could indeed enhance the cathodic ECL of $CsPbBr_3$/TDPA in aqueous solution.

Optimization of experimental conditions

In order to obtain optimal ECL response results, various experimental conditions were optimized as shown in Fig. 6. First, the scanning rate was optimized to select the best ECL response signal value between 60 and 140 mV s^{-1} (Fig. 7A). The resulting surface, without changing the rest of the conditions, can reach steady state when the scanning rate reaches 100 mV s^{-1}, with the highest ECL intensity. However, when the scanning rate exceeds 100 mV s^{-1}, the polarization speed of the electrode increases and the ECL intensity decreases. Secondly, the effect of $K_2S_2O_8$ concentration on ECL intensity was also investigated (Fig. 7B). The intensity of ECL increases with increasing concentration of $K_2S_2O_8$. When the concentration of $K_2S_2O_8$ reaches 120 mM, the ECL intensity reaches the maximum. However, when the

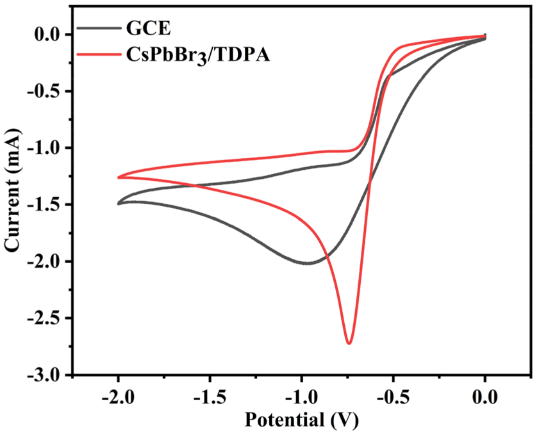

Fig. 6 CV responses of bare GCE and $CsPbBr_3$/TDPA NCs in 10 mM PBS containing 0.12 M $K_2S_2O_8$ and 0.1 mM nitrobenzene.

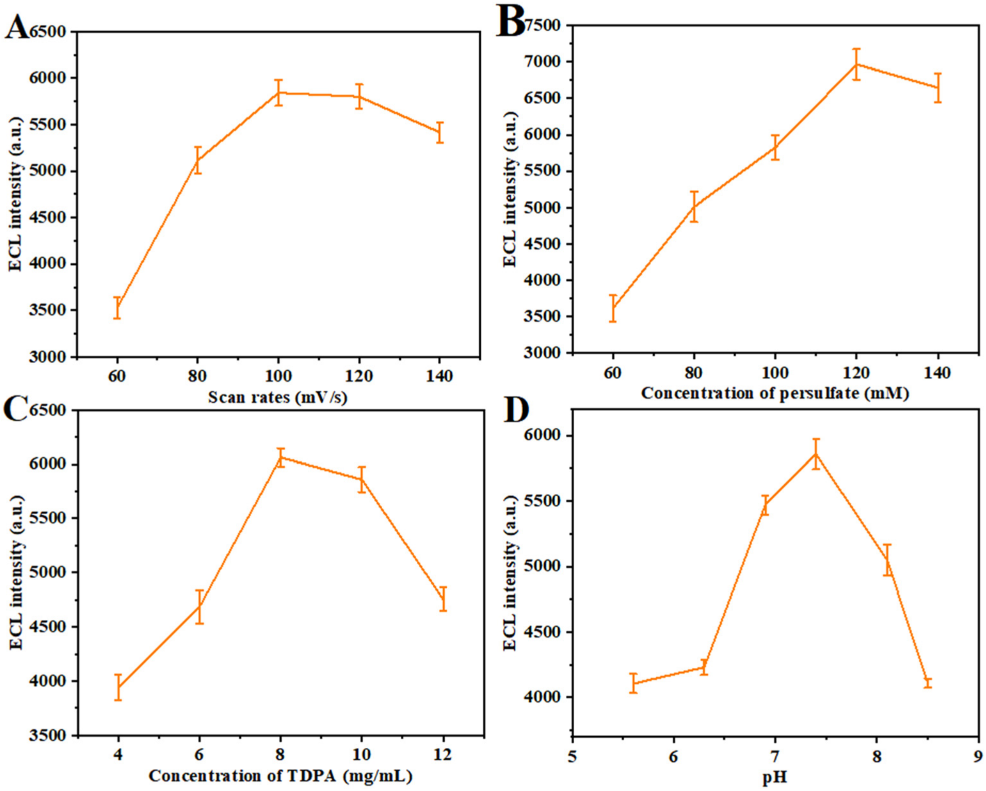

Fig. 7 Optimization of the experimental conditions: (A) scan rates, (B) concentration of persulfate, (C) concentration of TDPA, and (D) pH.

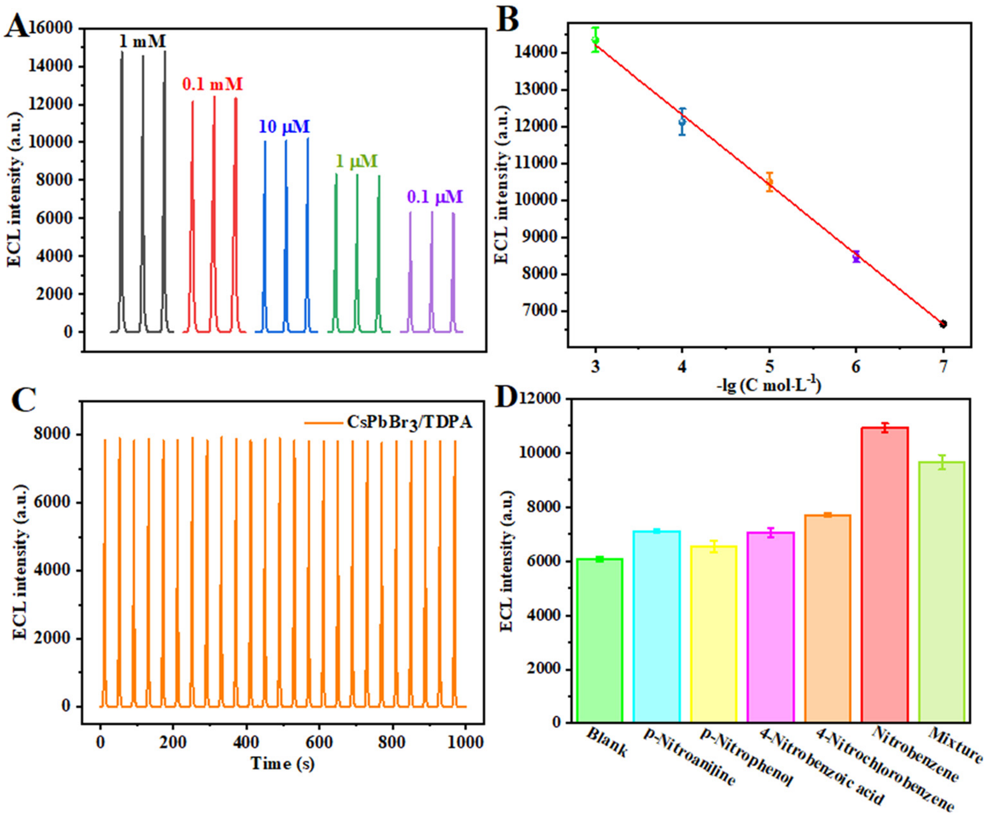

Fig. 8 (A) Calibration curve and (B) ECL response for different nitrobenzene levels. (C) The stability of the constructed ECL sensing platform for 25 scanning cycles. (D) The selectivity of the fabricated sensing platform for various targets.

Table 1 Comparison of this method with other methods reported in the literature

Material	Method	Linear range	LOD	Ref.
Zn-TDPAT	Fluorescence	50–5 × 10^3 ppm	50 ppm	39
$[Ln(mtpc)_{1.5}(DMA)(H_2O)]\cdot 2H_2O$	Fluorescence	15–150 ppm	15 ppm	40
Ln-MOFs	Fluorescence	0–0.7 mM	1.46 μM	41
Co-NC-800	DPV	0.1–63 μM	0.086 μM	42
EDAS/(g-C_3N_4-Ag)NC	CV	5–50 μM	2 μM	43
$CsPbBr_3$/TDPA	ECL	0.1–1 × 10^3 μM	0.05 μM	This work

concentration of $K_2S_2O_8$ exceeds 120 mM, too much $SO_4^{\bullet -}$ will be produced on the electrode surface, leading to the gradual reduction of ECL intensity. In addition, the effect of ligand concentration on ECL intensity was also investigated (Fig. 7C). When the ligand concentration is less than 8 mg mL^{-1}, the ECL intensity is low, which may be due to the poor passivation effect on the surface of $CsPbBr_3$ QDs. However, when the ligand concentration was greater than 8 mg mL^{-1}, the intensity of ECL decreased gradually. This is because the steric hindrance caused by the high concentration of TDPA leads to the generation of more unaligned atoms on the surface. Therefore, 8 mg mL^{-1} was chosen as the optimal ligand concentration. Finally, the effect of solution pH on ECL intensity was studied, and the experiment was carried out in the pH range of 5.5–8.5 (Fig. 7D). As the pH increases, the number of negatively charged species increases. In addition, the electron transfer speed is greatly accelerated, and the ECL intensity will also increase. At the same time, when the pH is greater than 7.4, too much negative charge will be deposited on the electrode surface, and the ECL intensity will also decrease. Therefore, 7.4 was chosen as the optimal pH.

Analytical performance of the ECL sensors

The ECL sensor was tested with different concentrations of nitrobenzene under the best experimental conditions. By the single variable method, the prepared $CsPbBr_3$/TDPA/GCE sensor platform was placed in a mixture of 120 mM $K_2S_2O_8$ and 10 mM PBS containing different concentrations of nitrobenzene for ECL analysis. As shown in Fig. 8A, with the increase of target concentration, the ECL response signal of the sensor gradually increases. In the range of nitrobenzene concentrations from 1 mM to 0.1 μM, the intensity of the ECL response signal was linearly related to the logarithm of nitrobenzene concentration (Fig. 8B). The linear fitting equation was $I = 188.1301\log C + 19\,865$, the correlation coefficient was 0.997, and the detection limit was 0.05 μM (S/N = 3). In fact, the LOD was calculated according to $3\sigma/S$, where σ is the standard deviation of three independent blank sample responses and S is the slope of the analytical curve. Compared with previous studies (Table 1), the established sensor has better performance.

Table 2 Measurement of TDPA in spiked samples

Serum sample	Added (μM)	Found (μM)	Recovery	RSD (%, n = 3)
1	0	0.11	0	2.87
2	1	0.97	0.97	0.96
3	10	10.3	1.03	2.56
4	100	10.1	1.01	0.63

Stability and selectivity of the sensor

It is well known that selectivity and stability are essential properties of excellent sensors. After 25 consecutive CV scanning cycles, the ECL intensity basically remained stable, indicating that the sensor had good stability (Fig. 8C). Meanwhile, in order to test the selectivity of the sensor, the ECL response characteristics of the sensor platform $CsPbBr_3$/TDPA/GCE were used to detect a variety of different substances. We measured and compared the ECL signal responses of *p*-nitroaniline, *p*-nitrophenol, 4-nitrobenzoic acid, 4-nitrochlorobenzene and nitrobenzene (Fig. 8D). The concentration of all substances was 10 μM. Compared with the ECL intensity of the blank solution, the ECL intensity increased slightly with the interfering substances. At the same time, the ECL intensity of nitrobenzene increased obviously. In the detection of mixed samples, the signal corresponding to the ECL sensor is equivalent to the signal of the 10 μM nitrobenzene sample. Nitrobenzene has greater flexibility and smaller steric hindrance than the other detected substances. The orientation of other interfering materials may deviate substantially from the vertical direction, disrupting π–π stacking and reducing electron delocalization. At the same time, nitrobenzene, as a compound rich in π electrons, has a stronger interaction with the surface of the perovskite, and the intercalation configuration is less affected, so the constructed sensor has good selectivity. The results show that the $CsPbBr_3$/TDPA/GCE sensor has good selectivity to nitrobenzene.

Detection of real samples

The sensor platform $CsPbBr_3$/TDPA/GCE was used for the detection of real samples to evaluate the practical detection capability of the sensor platform. A tap water sample was tested, and a recovery experiment was carried out by the standard addition method, and then three different concentrations of samples were measured under the same conditions and the recovery of nitrobenzene was calculated. The results are shown in Table 2, and the recoveries are 97%, 101% and 103%, respectively, which proves that the sensor has high accuracy in real environmental samples.

Conclusion

In this work, TDPA-coated $CsPbBr_3$ QDs were synthesized by recrystallization at room temperature. Compared with those of unmodified $CsPbBr_3$ QDs, the water stability and ECL response signal of the composite are greatly improved, and the ECL stability and reproducibility are also enhanced. ECL analysis based on $CsPbBr_3$ QDs is performed in the aqueous phase, which expands its application in biological analysis. More importantly, it greatly improves the electrochemical performance of $CsPbBr_3$ QDs and has more excellent electrical conductivity. It is found that nitrobenzene can effectively enhance the ECL response signal generated in a $CsPbBr_3$/TDPA–$K_2S_2O_8$ system. Based on this, an ECL sensor platform for nitrobenzene detection was prepared. In this work, the cathodic ECL of perovskite nanocrystals in aqueous solution was explored, and its potential application in ECL sensors and nanodevices was expanded.

Conflicts of interest

There are no conflicts to declare.

Acknowledgements

This work was supported by the National Natural Science Foundation of China (21976001), the University Collaborative Innovation Project of Anhui Province (GXXT-2019-023) and the Natural Science Research Projects of Universities in Anhui Province (KJ2021A0030).

References

1 Y. Salinas, R. Martínez-Máñez, M. D. Marcos, F. Sancenón, A. M. Costero, M. Parra and S. Gil, Optical chemosensors and reagents to detect explosives, *Chem. Soc. Rev.*, 2012, **41**(3), 1261–1296.

2 X. Yan, H. Wang, C. E. Hauke, T. R. Cook, M. Wang, M. L. Saha, Z. Zhou, M. Zhang, X. Li, F. Huang and P. J. Stang, A Suite of Tetraphenylethylene-Based Discrete Organoplatinum(II) Metallacycles: Controllable Structure and Stoichiometry, Aggregation-Induced Emission, and Nitroaromatics Sensing, *J. Am. Chem. Soc.*, 2015, **137**(48), 15276–15286.

3 A. Ayati, B. Tanhaei, F. F. Bamoharram, A. Ahmadpour, P. Maydannik and M. Sillanpää, Photocatalytic degradation of nitrobenzene by gold nanoparticles decorated polyoxometalate immobilized TiO_2 nanotubes, *Sep. Purif. Technol.*, 2016, **171**, 62–68.

4 B. Thirumalraj, S. Palanisamy, S.-M. Chen, K. Thangavelu, P. Periakaruppan and X.-H. Liu, A simple electrochemical platform for detection of nitrobenzene in water samples using an alumina polished glassy carbon electrode, *J. Colloid Interface Sci.*, 2016, **475**, 154–160.

5 L. Zhai, Z.-X. Yang, W.-W. Zhang, J.-L. Zuo and X.-M. Ren, Dual-emission and thermochromic luminescence alkaline earth metal coordination polymers and their blend films with polyvinylidene fluoride for detecting nitrobenzene vapor, *J. Mater. Chem. C*, 2018, **6**(26), 7030–7041.

6 P. Yu, L. Chen, Y. Zhang, S. Zhao, Z. Chen, Y. Hu, J. Liu, Y. Yang, J. Shi, Z. Yao and W. Hong, Single-Molecule Tunneling Sensors for Nitrobenzene Explosives, *Anal. Chem.*, 2022, **94**(35), 12042–12050.

7 Z. Liu, W. Qi and G. Xu, Recent advances in electrochemiluminescence, *Chem. Soc. Rev.*, 2015, **44**(10), 3117–3142.

8 M.-F. Lo, Z.-Q. Guan, T.-W. Ng, C.-Y. Chan and C.-S. Lee, Electronic Structures and Photoconversion Mechanism in Perovskite/Fullerene Heterojunctions, *Adv. Funct. Mater.*, 2015, **25**(8), 1213–1218.

9 G. Li, F. W. R. Rivarola, N. J. L. K. Davis, S. Bai, T. C. Jellicoe, F. de la Peña, S. Hou, C. Ducati, F. Gao, R. H. Friend, N. C. Greenham and Z.-K. Tan, Highly Efficient Perovskite Nanocrystal Light-Emitting Diodes Enabled by a Universal Crosslinking Method, *Adv. Mater.*, 2016, **28**(18), 3528–3534.

10 Q. Liao, K. Hu, H. Zhang, X. Wang, J. Yao and H. Fu, Perovskite Microdisk Microlasers Self-Assembled from Solution, *Adv. Mater.*, 2015, **27**(22), 3405–3410.

11 H. Zhang, Q. Liao, X. Wang, K. Hu, J. Yao and H. Fu, Controlled Substitution of Chlorine for Iodine in Single-Crystal Nanofibers of Mixed Perovskite $MAPbI_3$-xClx, *Small*, 2016, **12**(28), 3780–3787.

12 Y. Liu, X. Tang, T. Zhu, M. Deng, I. P. Ikechukwu, W. Huang, G. Yin, Y. Bai, D. Qu, X. Huang and F. Qiu, All-inorganic $CsPbBr_3$ perovskite quantum dots as a photoluminescent probe for ultrasensitive Cu^{2+} detection, *J. Mater. Chem. C*, 2018, **6**(17), 4793–4799.

13 Z. Li, Q. Kang, L. Chen, B. Zhang, G. Zou and D. Shen, Enhancing aqueous stability and radiative-charge-transfer efficiency of $CsPbBr_3$ perovskite nanocrystals via conductive silica gel coating, *Electrochim. Acta*, 2020, **330**, 135332.

14 C. Zhao, Z. He, P. Wangyang, J. Tan, C. Shi, A. Pan, L. He and Y. Liu, Bidentate Ligand-Induced Oriented Transformation of $CsPbBr_3$ Perovskite Nanocrystals into Nanowires for X-ray Photodetectors, *ACS Appl. Nano Mater.*, 2022, **5**(10), 13737–13744.

15 B. Zhang, L. Goldoni, J. Zito, Z. Dang, G. Almeida, F. Zaccaria, J. de Wit, I. Infante, L. De Trizio and L. Manna, Alkyl Phosphonic Acids Deliver $CsPbBr_3$ Nanocrystals with High Photoluminescence Quantum Yield and Truncated Octahedron Shape, *Chem. Mater.*, 2019, **31**(21), 9140–9147.

16 L. Protesescu, S. Yakunin, M. I. Bodnarchuk, F. Krieg, R. Caputo, C. H. Hendon, R. X. Yang, A. Walsh and M. V. Kovalenko, Nanocrystals of Cesium Lead Halide Perovskites ($CsPbX_3$, X = Cl, Br, and I): Novel Optoelectronic Materials Showing Bright Emission with Wide Color Gamut, *Nano Lett.*, 2015, **15**(6), 3692–3696.

17 L. Wu, M. Zhang, S. Yang, R. Wu, S. Gong, Q. Han and W. Wu, Spectral and dynamic analysis of $CsPbBr_3$ perovskite nanocrystals with enhanced water stability using sodium passivation, *J. Alloys Compd.*, 2021, **889**, 161721.

18 K. A. Fähnrich, M. Pravda and G. G. Guilbault, Recent applications of electrogenerated chemiluminescence in chemical analysis, *Talanta*, 2001, **54**(4), 531–559.

19 L. Li, Y. Chen and J.-J. Zhu, Recent Advances in Electrochemiluminescence Analysis, *Anal. Chem.*, 2017, **89**(1), 358–371.

20 L. Li, Z. Zhang, Y. Chen, Q. Xu, J.-R. Zhang, Z. Chen, Y. Chen and J.-J. Zhu, Sustainable and Self-Enhanced Electrochemiluminescent Ternary Suprastructures Derived from $CsPbBr_3$ Perovskite Quantum Dots, *Adv. Funct. Mater.*, 2019, **29**(32), 1902533.

21 Y. Huang, X. Long, D. Shen, G. Zou, B. Zhang and H. Wang, Hydrogen Peroxide Involved Anodic Charge Transfer and Electrochemiluminescence of All-Inorganic Halide Perovskite $CsPbBr_3$ Nanocrystals in an Aqueous Medium, *Inorg. Chem.*, 2017, **56**(17), 10135–10138.

22 J. Ballesta-Claver, R. Rodríguez-Gómez and L. F. Capitán-Vallvey, Disposable biosensor based on cathodic electrochemiluminescence of tris(2,2-bipyridine) ruthenium(II) for uric acid determination, *Anal. Chim. Acta*, 2013, **770**, 153–160.

23 Q. Jun-e, C. Geng, W. Hai-ren and C. Zhi-yong, The protection of TDPA deposited from mixed solutions with different water/ethanol ratios for aluminum alloy against corrosion in NaCl solution, *Anti-Corros. Methods Mater.*, 2017, **64**(2), 233–240.

24 H. Asbaghian-Namin, P. Karami, H. Naghshara, D. Gholamin and M. Johari-Ahar, Electrochemiluminescent immunoassay for the determination of CA15-3 and CA72-4 using graphene oxide nanocomposite modified with CdSe quantum dots and $Ru(bpy)_3$ complex, *Microchim. Acta*, 2021, **188**(7), 238.

25 X. Wang, H. Liu, H. Qi, Q. Gao and C. Zhang, Highly efficient electrochemiluminescence of ruthenium complex-functionalized CdS quantum dots and their analytical application, *J. Mater. Chem. B*, 2020, **8**(16), 3598–3605.

26 L. Fu, X. Gao, S. Dong, J. Jia, Y. Xu, D. Wang and G. Zou, Coreactant-Free and Direct Electrochemiluminescence from Dual-Stabilizer-Capped InP/ZnS Nanocrystals: A New Route Involving n-Type Luminophore, *Anal. Chem.*, 2022, **94**(2), 1350–1356.

27 L. Chen, X. Zeng, P. Si, Y. Chen, Y. Chi, D.-H. Kim and G. Chen, Gold Nanoparticle-Graphite-Like C_3N_4 Nanosheet Nanohybrids Used for Electrochemiluminescent Immunosensor, *Anal. Chem.*, 2014, **86**(9), 4188–4195.

28 H. Gao, S. Liu, Z. Xue, W. Liu, Y. Nie, G. Chen and X. Li, Synthesis and photoluminescence properties of $CsPbBr_3$ quantum dots by using para-xylene as the anti-solvent, *J. Lumin.*, 2019, **215**, 116584.

29 T. Xuan, X. Yang, S. Lou, J. Huang, Y. Liu, J. Yu, H. Li, K.-L. Wong, C. Wang and J. Wang, Highly stable $CsPbBr_3$ quantum dots coated with alkyl phosphate for white light-emitting diodes, *Nanoscale*, 2017, **9**(40), 15286–15290.

30 C. Sun, Y. Zhang, C. Ruan, C. Yin, X. Wang, Y. Wang and W. W. Yu, Efficient and Stable White LEDs with Silica-Coated Inorganic Perovskite Quantum Dots, *Adv. Mater.*, 2016, **28**(45), 10088–10094.

31 F. Wang, H. Wang, A. Ali, Y. Zhang, X. Cui and Y. Liu, In-situ one-step electrospray fabrication of polyvinylidene fluoride encapsulated $CsPbBr_3$ spheres with high stability and cell imaging application, *Inorg. Chem. Commun.*, 2019, **106**, 99–103.

32 J.-E. Qu, G. Chen, H.-R. Wang and D.-J. Nie, Effect of water content on corrosion inhibition behavior of self-assembled TDPA on aluminum alloy surface, *Trans. Nonferrous Met. Soc. China*, 2013, **23**(10), 3137–3144.

33 H.-D. Nguyen, C. C. Lin and R.-S. Liu, Waterproof Alkyl Phosphate Coated Fluoride Phosphors for Optoelectronic Materials, *Angew. Chem., Int. Ed.*, 2015, **54**(37), 10862–10866.

34 J. Han, M. Sharipov, S. Hwang, Y. Lee, B. T. Huy and Y.-I. Lee, Water-stable perovskite-loaded nanogels containing antioxidant property for highly sensitive and selective detection of roxithromycin in animal-derived food products, *Sci. Rep.*, 2022, **12**(1), 3147.

35 H. Dai, X. Wu, Y. Wang, W. Zhou and G. Chen, An electrochemiluminescent biosensor for vitamin C based on inhibition of luminol electrochemiluminescence on graphite/poly(methylmethacrylate) composite electrode, *Electrochim. Acta*, 2008, **53**(16), 5113–5117.

36 K. Hills-Kimball, H. Yang, T. Cai, J. Wang and O. Chen, Recent Advances in Ligand Design and Engineering in Lead Halide Perovskite Nanocrystals, *Adv. Sci.*, 2021, **8**(12), 2100214.

37 A. Ioakeimidis and S. A. Choulis, Nitrobenzene as Additive to Improve Reproducibility and Degradation Resistance of Highly Efficient Methylammonium-Free Inverted Perovskite Solar Cells, *Materials*, 2020, **13**(15), 3289.

38 J. Xue, R. Wang, X. Chen, C. Yao, X. Jin, K.-L. Wang, W. Huang, T. Huang, Y. Zhao, Y. Zhai, D. Meng, S. Tan, R. Liu, Z.-K. Wang, C. Zhu, K. Zhu, M. C. Beard, Y. Yan and Y. Yang, Reconfiguring the band-edge states of photovoltaic perovskites by conjugated organic cations, *Science*, 2021, **371**(6529), 636–640.

39 D. Ma, B. Li, X. Zhou, Q. Zhou, K. Liu, G. Zeng, G. Li, Z. Shi and S. Feng, A dual functional MOF as a luminescent sensor for quantitatively detecting the concentration of nitrobenzene and temperature, *Chem. Commun.*, 2013, **49**(79), 8964–8966.

40 X.-M. Cao, N. Wei, L. Liu, L. Li and Z.-B. Han, Luminescent lanthanide-organic polyrotaxane framework as a turn-off sensor for nitrobenzene and Fe^{3+}, *RSC Adv.*, 2016, **6**(23), 19459–19462.

41 Z. Sun, J. Sun, L. Xi, J. Xie, X. Wang, Y. Ma and L. Li, Two Novel Lanthanide Metal-Organic Frameworks: Selective Luminescent Sensing for Nitrobenzene, Cu^{2+}, and MnO^{4-}, *Cryst. Growth Des.*, 2020, **20**(8), 5225–5234.

42 S. An, N. Shang, J. Zhang, A. Nsabimana, M. Su, S. Zhang and Y. Zhang, Fabrication of electrocatalytically active, cobalt-embedded nitrogen-doped ordered macroporous carbon for sensitive detection of nitrobenzene, *Colloids Surf., A*, 2022, **653**, 130078.

43 C. Pandiyarajan, P. Rameshkumar, S. Murugesan and M. Selvaraj, Silver nanoparticles-supported graphitic-like carbon nitride for the electrochemical sensing of nitrobenzene and its derivatives, *J. Mater. Sci.: Mater. Electron.*, 2021, **32**(14), 19912–19924.